UNIVERSITÀ DEGLI STUDI DI PADOVA

Dipartimento di Fisica e Astronomia "Galileo Galilei"

Corso di Laurea in Fisica

Tesi di Laurea

Optimal Control of Superconducting Qubit Gates

Relatore   Laureando

Prof. Simone Montangero   Paolo Zinesi

Anno Accademico 2020/2021

Abstract

Quantum technologies promise to improve the performance of a whole range of computational processes. This is why researchers have been studying the physical implementation of such technologies for over 30 years.

One of the most well-established platforms to perform quantum calculations are superconducting qubits, in which Cooper pairs tunnel across insulating barriers that separate superconductors.

After introducing superconductivity theory, we simulate one- and two-qubit gates by controlling applied voltages and magnetic fields. Then, we show how an external noise source can alter the behavior of the quantum gate.

Finally, we apply optimal control theory to find the time-dependent voltage and magnetic fields that maximize the target gate's success probability. With this procedure we aim to compensate for the experimental imperfections via a general numerical approach.

Contents

Introduction

Richard Feynman in 1982 introduced the idea of a quantum computer, a new kind of computer that can simulate quantum systems efficiently [1]. Feynman's work builds from the fact that the exact simulation of quantum systems with universal classical computers is not always possible. In fact, a theory which reproduces quantum mechanical predictions needs to have a non-local structure [2]. Classical computers follow the rules of classical physics, which is a local theory, while quantum physics admit the existence of non-local correlations between entangled particles. So, we need computers that follows quantum mechanics to simulate all the possible quantum systems.

Since then, quantum technologies progressed considerably and a variety of dedicated software and hardware have been developed. Researchers found out that quantum mechanical properties, such as superposition and entanglement, can speed up some expensive tasks in certain algorithms. As an example, the Quantum Fourier Transform (QFT) algorithm [3] computes the discrete Fourier transform in polynomial time with respect to the input size, while the classical Fast Fourier Transform (FFT) algorithm needs exponential time.

The physical realization of a platform that can run such algorithms is one of the main challenges that quantum technologies have to overcome. Experimental imperfections and, eventually, interactions with the environment affect the state of the system, giving rise to errors. The quality of the quantum hardware depends on both the number of qubits, the two-state quantum systems, and the error rate of the setup.

In this thesis we concentrate on superconducting qubits as a possible implementation of quantum computers. The superconducting qubits are based on devices called Josephson junctions, in which pairs of electrons tunnel across a thin insulating barrier that separates two superconductors. Under suitable conditions, the Josephson junction reduces to a two-state system that can be used for quantum computation [4]. Operations on single qubits are performed by tuning voltages and magnetic fields and the coupling between two qubits provides the necessary two-qubit operations.

Enterprises such as Google [5], IBM [6], Rigetti [7], are now developing commercial processors with more than 50 qubits using superconducting circuits. These processors allow to implement universal quantum computation and Google claimed in 2019 to have reached quantum supremacy using a 53-qubit processor [8]. Nevertheless, D-Wave announced in 2019 a 5000-qubit processor [9] specialized in quantum annealing but unable to support generic quantum computation. The results obtained by the scientific community attract investments and make the superconducting technologies a flourishing research field.

One important part of the experimental research work is focused on the construction of apparatus that are more robust against external dephasing sources. This goal can be achieved, for instance, by improving electromagnetic shielding or the cryogenic apparatus. Another solution to reduce dephasing effects in the processor comes from mathematical optimization. Quantum Optimal Control (QOC) [10–12] uses the tools of Optimal Control Theory to find the time-dependent control pulses that minimize a specific cost function J. That function J depends on the goal of the optimization. The optimal control pulses allow to obtain gates that are less influenced by environmental noise and experimental imperfections.

In the first chapter of the thesis we introduce the theory of superconductivity, starting from the early experimental observations and presenting the empirical London equations to explain them. Then, we present the basic concepts of the BCS theory and we describe the characteristics of the BCS ground state. From these results we present a derivation of the second London equation.

In the second chapter we describe how the theory of superconductivity enables the construction of superconducting qubits using Josephson junctions. A simple theoretical explanation of the Josephson effect is presented. We then describe the properties of charge qubits and a possible real-world implementation of qubit gates.

Finally, in the third chapter we add an external noise source to the implementation of the second chapter and we observe the deviations of the gates from the expected behavior. Then, we use Quantum Optimal Control to implement gates that are robust against external noise sources.

Chapter 1

Introduction to Superconductivity Theory

1.1 First experimental observations

Many metals and alloys below a critical temperature T_C show no electrical resistivity. This phenomenon is called *superconductivity*. At the critical temperature, a phase transition from a normal conducting state to a superconducting state occurs.

This phenomenon was observed for the first time by physicist Kamerlingh Onnes in 1911 while he was working with pure mercury in liquid helium temperatures [13]. Onnes measured the resistance at different temperatures and compared it to the resistance at $T = 0$°C. While the resistance at $T = 4.3\,\text{K}$ was 0.21% of the resistance at 0°C, at $T = 3\,\text{K}$ the resistance dropped below 10^{-7} times the resistance at 0°C. A persistent current can thus flow in a superconducting ring for a very long time without attenuation.

Superconductors exhibit also peculiar magnetic properties at temperatures below T_C. It is possible to show experimentally that a bulk superconductor in a weak magnetic field behaves as an exact diamagnet. As soon as an external magnetic field $\boldsymbol{B_{ext}}$ is switched on, persistent surface currents start to flow and generate an opposite magnetic field, giving net zero magnetic field on the inside of the superconductor. Nevertheless, if a normal conductor in a weak magnetic field is cooled down to its critical temperature, the magnetic field in the material is expelled. This phenomenon is the *Meissner effect*. This effect is visible for magnetic fields below a temperature-dependent critical magnetic field $B_C(T)$, while for stronger magnetic fields the materials return to the normal conducting state.

The observation of such an effect demonstrates that the superconductors cannot be simply described as materials with vanishing resistivity ρ below the critical temperature. In fact, in classical electromagnetism Ohm's law states

$$\boldsymbol{E} = \rho\,\boldsymbol{j}. \tag{1.1}$$

If ρ tends to zero and if the current density $\boldsymbol{j}$ stays finite, the electric field $\boldsymbol{E}$ has to vanish. If $\boldsymbol{E}$ vanishes, according to the Maxwell's equation

$$\boldsymbol{\nabla} \times \boldsymbol{E} = -\frac{\partial \boldsymbol{B}}{\partial t}, \tag{1.2}$$

also $\frac{\partial \boldsymbol{B}}{\partial t} = 0$ and thus the magnetic field $\boldsymbol{B}$ is constant. This simplistic description of the superconductor implies that, after the cooling, the magnetic field should stay constant inside the bulk superconductor even if the external field is switched off. But the experiments disagree with this simple description. The real superconductor below T_C presents no magnetic field on the inside and if a magnetic field was in the material before the cooling, when the temperature goes below T_C the field is gradually expelled.

1.2 London equations

Fritz London and Heinz London proposed in 1935 a set of phenomenological equations to explain the relation between superconducting currents and magnetic fields [14]. The London equations replace Ohm's law in the description of a superconductor and give the expected experimental results. A

simplified derivation of the London equations is now presented.

We consider at first the classical equation of motion of an electron in an external electric field $\boldsymbol{E}$,

$$m\dot{\boldsymbol{v}} + \frac{m}{\tau_R}\boldsymbol{v_D} = -e\boldsymbol{E}. \tag{1.3}$$

In Eq. (1.3) m is the mass of an electron, $\boldsymbol{v_D}$ is the difference between the electron velocity $\boldsymbol{v}$ and the thermal velocity $\boldsymbol{v}_{\text{therm}}$, and τ_R is the characteristic time at which $\boldsymbol{v}$ relaxes exponentially to $\boldsymbol{v}_{\text{therm}}$ when the external field is zero.

We take into account the vanishing resistivity by neglecting the friction term $m\boldsymbol{v_D}/\tau_R$. With the definition of the current density $\boldsymbol{j_s} = -en_s\boldsymbol{v}$, for superconducting electrons of density n_s, the first London equation follows

$$\frac{\partial \boldsymbol{j_s}}{\partial t} = \frac{n_s e^2}{m}\boldsymbol{E}. \tag{1.4}$$

Computing the curl on both sides of Eq. (1.4) and using Eq. (1.2) to get an expression for the magnetic field, we get

$$\frac{\partial}{\partial t}\left(\boldsymbol{\nabla}\times\boldsymbol{j_s}\right) = \frac{n_s e^2}{m}\left(-\frac{\partial\boldsymbol{B}}{\partial t}\right),$$

$$\frac{\partial}{\partial t}\left(\boldsymbol{\nabla}\times\boldsymbol{j_s} + \frac{n_s e^2}{m}\boldsymbol{B}\right) = 0. \tag{1.5}$$

Equation (1.5) can be integrated over time and an integration constant appears. In order to get the equation that correctly describes the Meissner effect, this constant must be set equal to zero. The second London equation is thus

$$\boldsymbol{\nabla}\times\boldsymbol{j_s} + \frac{n_s e^2}{m}\boldsymbol{B} = 0. \tag{1.6}$$

Equations (1.4) and (1.6) describe the relation between $\boldsymbol{E}, \boldsymbol{B}, \boldsymbol{j_s}$ in a superconductor and they are the superconducting version of Ohm's law.

The combination of the London equations with the Maxwell's equations in static conditions

$$\boldsymbol{\nabla}\times\boldsymbol{B} = \mu_0\boldsymbol{j_s}, \tag{1.7}$$

$$\boldsymbol{\nabla}\cdot\boldsymbol{B} = 0, \tag{1.8}$$

yields the differential equation

$$\boldsymbol{\nabla}^2\boldsymbol{B} - \frac{\mu_0 n_s e^2}{m}\boldsymbol{B} = 0. \tag{1.9}$$

Considering a semi-infinite superconductor along $z > 0$ and a magnetic field that on the surface $z = 0$ is $\boldsymbol{B} = B_0\,\hat{\boldsymbol{x}}$, a possible solution of Eq. (1.9) has the form

$$\boldsymbol{B} = B_0\,e^{-z/\Lambda_L}\,\hat{\boldsymbol{x}}, \tag{1.10}$$

where $\Lambda_L = \sqrt{\frac{m}{\mu_0 n_s e^2}}$ is defined as the London penetration depth in the superconductor. The solutions proportional to e^{+z/Λ_L} are divergent and so they are not further considered. The same calculations bring to an identical solution for the current density $\boldsymbol{j_s}$. Magnetic fields of the form of Eq. (1.10) are exponentially suppressed inside the superconductor with a characteristic length scale of Λ_L. An estimate of Λ_L can be obtained setting n_s as the atomic density. For example, $\Lambda_L = 160\,\text{Å}$ for Aluminium and $\Lambda_L = 1110\,\text{Å}$ for Cadmium [15]. In macroscopic superconductors Eq. (1.10) implies the absence of any magnetic field after a thin layer of material.

1.3   BCS theory

In 1956 Leon N. Cooper demonstrated that, in the presence of a Fermi sphere of additional electrons, the Pauli exclusion principle allows the existence of a two-electron bound state independently from the weakness of the attraction between the electrons [16]. In the famous 1957 paper of Bardeen, Cooper

and Schrieffer (BCS), an attractive interaction emerges in the form of phonon-mediated interaction [17]. An electron passing through a lattice deforms slightly the position of the positive ions and this effect increases the density of positive charge around the lattice ions. This increment has an attractive effect on a second electron. The slow displacement of an ion core (i.e., the attraction on a second electron) is maximum when the first electron is at a distance of more than $1000\,\text{Å}$. The Coulomb repulsion of the electrons is completely screened over such distances.

The pairs of electrons that interact via the electron-lattice-electron mechanism are called *Cooper pairs*. All Cooper pairs occupy states $(\boldsymbol{k}\uparrow, -\boldsymbol{k}\downarrow)$, with opposite wavevectors $\boldsymbol{k}$ and spins $\uparrow\downarrow$ to satisfy the exclusion principle. The scattering of a Cooper pair from $(\boldsymbol{k}\uparrow, -\boldsymbol{k}\downarrow)$ to $(\boldsymbol{k}'\uparrow, -\boldsymbol{k}'\downarrow)$ leads to an energy reduction, since the matrix element $V_{\boldsymbol{k},\boldsymbol{k}'}$ is attractive and independent of $\boldsymbol{k}$ to a first approximation. In fact, BCS theory uses a potential of the form

$$V_{\boldsymbol{k},\boldsymbol{k}'} = \begin{cases} -V_0 & \text{for } 0 < \frac{\hbar^2 k^2}{2m} - E_F < \hbar\omega_D \text{ and } 0 < \frac{\hbar^2 k'^2}{2m} - E_F < \hbar\omega_D \\ 0 & \text{otherwise} \end{cases}. \tag{1.11}$$

The Fermi energy E_F is the energy of the highest occupied state of the electrons gas at $T = 0\,\text{K}$. The Debye frequency ω_D is the average phonon frequency of the material in the Debye model. The positive constant V_0 represents the intensity of the attraction between two electrons, and when V_0 tends to zero the non-interacting electrons gas results are obtained.

The energy reduction caused by the formation of a Cooper pair leads to the formation of even more Cooper pairs, until a new ground state is reached. This new ground state is separated by a finite energy gap $E_g \equiv 2\Delta$ from the first excited state, and it is precisely a superconducting state. Although based on strong approximations, the results of BCS theory are in good agreement with a large class of superconductors [15].

In the following we briefly review some of the major theoretical results obtained by BCS theory. The energy gap Δ of a superconductor is defined as half of the minimum energy needed to break a Cooper pair of electrons in the ground state at $T = 0\,\text{K}$. However, the energy gap ultimately depends on the constant V_0 and on a $\boldsymbol{k}$-summation of state-occupancy probabilities. Defining $Z(E_F)$ as the pair density of states at the Fermi energy and performing the $\boldsymbol{k}$-summation, an explicit equation for Δ can be obtained

$$\Delta = \frac{\hbar\omega_D}{\sinh\left(1/V_0\,Z(E_F)\right)} \approx 2\hbar\omega_D e^{-1/V_0\,Z(E_F)}. \tag{1.12}$$

In Eq. (1.12) we can notice that a finite V_0 leads to a finite energy gap in the material, while a vanishing V_0 causes the energy gap to close. In addition, the value of Δ is directly proportional to the average phonon energy $\hbar\omega_D$.

At temperatures above $T = 0\,\text{K}$ there is a finite probability to find electrons in the normal conducting state because of thermal excitations. That probability increases for greater temperatures until at the critical temperature T_C all the Cooper pairs are separated. At that temperature the superconductor transforms into a normal conductor and the gap is closed. This condition can be expressed as

$$\frac{1}{V_0\,Z(E_F)} = \int_0^{\hbar\omega_D} \frac{1}{\epsilon}\tanh\left(\frac{\epsilon}{2k_B T_C}\right)d\epsilon. \tag{1.13}$$

The numerical solution of the integral gives

$$k_B T_C = 1.14\,\hbar\omega_D\,e^{-1/V_0\,Z(E_F)}. \tag{1.14}$$

1.3.1 Demonstration of the second London equation

We report now a calculation of the density of a supercurrent $\boldsymbol{j_s}$ in a magnetic field $\boldsymbol{B}$ that uses the results of BCS theory [18].

The many-particle wave function of a superconductor is a product of two-particle wave functions of Cooper pairs $\psi(\boldsymbol{x}_1, \boldsymbol{x}_2)$. More precisely, the many-particle wave function is a normalized sum of such two-particle wave function products. In the presence of a current flow, the Cooper pair wave function can be written as

$$\psi(\boldsymbol{x}_1, \boldsymbol{x}_2) = e^{i\boldsymbol{K}\cdot\boldsymbol{R}}\,\psi(\boldsymbol{K} = 0; \boldsymbol{x}_1 - \boldsymbol{x}_2), \tag{1.15}$$

in which $\hbar \boldsymbol{K}$ is the additional momentum of the Cooper pair due to the current flow, $\boldsymbol{R} = (\boldsymbol{x}_1 + \boldsymbol{x}_2)/2$ is the center of mass coordinate of the Cooper pair, and $\psi(\boldsymbol{K} = 0; \boldsymbol{x}_1 - \boldsymbol{x}_2)$ refers to the wave function without current flow. The wave function $\psi(\boldsymbol{K} = 0; \boldsymbol{x}_1 - \boldsymbol{x}_2)$ depends only on the relative coordinate $\boldsymbol{r} = \boldsymbol{x}_1 - \boldsymbol{x}_2$ of the electrons. The many-particle wave function is thus

$$\Psi_{BCS} = \hat{\mathcal{A}} \, e^{i\boldsymbol{K} \cdot (\boldsymbol{R}_1 + \boldsymbol{R}_2 + \cdots)} \Psi(\boldsymbol{K} = 0; \boldsymbol{r}_1, \boldsymbol{r}_2, \dots), \tag{1.16}$$

where $\hat{\mathcal{A}}$ is the anti-symmetrization operator, which adds expression similar to its argument with varying signs. The total wave function Ψ_{BCS} is thus antisymmetric for the exchange of single-particle states, as requested by the exclusion principle. Although being mathematically correct, the presence of the anti-symmetrization operator $\hat{\mathcal{A}}$ does not play a fundamental role in the following calculations and so it will be ignored. Defining $\Psi(\boldsymbol{K} = 0; \boldsymbol{r}_1, \boldsymbol{r}_2, \dots) = \Psi(0)$, Eq. (1.16) can be written as

$$\Psi_{BCS} \simeq e^{i\boldsymbol{K} \cdot (\boldsymbol{R}_1 + \boldsymbol{R}_2 + \cdots)} \Psi(0). \tag{1.17}$$

We can now define

$$\tilde{\boldsymbol{R}} = \frac{\sum_\nu \boldsymbol{R}_\nu}{\sum_\nu 1} = \frac{1}{N_{CP}} \sum_\nu \boldsymbol{R}_\nu, \qquad\qquad \tilde{\boldsymbol{K}} = \boldsymbol{K} \sum_\nu 1 = N_{CP} \boldsymbol{K}, \tag{1.18}$$

and then Eq. (1.17) becomes

$$\Psi_{BCS} \simeq e^{i\tilde{\boldsymbol{K}} \cdot \tilde{\boldsymbol{R}}} \Psi(0). \tag{1.19}$$

In the approximation of considering the set of N_{CP} Cooper pairs as a unique particle of total mass $M = 2mN_{CP}$ and total charge $Q = -2eN_{CP}$, the supercurrent density $\boldsymbol{j_s}$ is related to the current density of probability $\boldsymbol{\mathcal{J}}$ by the relation

$$\boldsymbol{j_s} = Q\boldsymbol{\mathcal{J}}, \tag{1.20}$$

and $\boldsymbol{\mathcal{J}}$ has the well-known definition [19, p. 314]

$$\boldsymbol{\mathcal{J}} = \frac{1}{M} Re \left\{ \Psi^* \left[\frac{\hbar}{i} \hat{\boldsymbol{\nabla}} - Q\boldsymbol{A} \right] \Psi \right\}, \tag{1.21}$$

in which $\boldsymbol{A}$ is the magnetic vector potential. Applying Eq. (1.20) and (1.21) to Ψ_{BCS} we get a relation for the supercurrent density

$$\begin{aligned} \boldsymbol{j_s} &= \frac{Q}{M} Re \left\{ \Psi_{BCS}^* \left[\frac{\hbar}{i} \hat{\boldsymbol{\nabla}}_{\tilde{\boldsymbol{R}}} - Q\boldsymbol{A} \right] \Psi_{BCS} \right\} \\ &= -\frac{e}{m} \left[\hbar\tilde{\boldsymbol{K}} + 2eN_{CP}\boldsymbol{A} \right] |\Psi(0)|^2. \end{aligned} \tag{1.22}$$

Since $\boldsymbol{\nabla} \times \tilde{\boldsymbol{K}} = 0$ because $\tilde{\boldsymbol{K}}$ does not depend on space coordinates, the application of the curl on both sides of Eq. (1.22) gives

$$\boldsymbol{\nabla} \times \boldsymbol{j_s} = -\frac{e^2}{m} 2N_{CP} |\Psi(0)|^2 \left(\boldsymbol{\nabla} \times \boldsymbol{A} \right) = -\frac{n_s e^2}{m} \boldsymbol{B}, \tag{1.23}$$

defining $|\Psi(0)|^2 = 1/V$ for the $\Psi(0)$ normalization condition. Thus $n_s = 2N_{CP}/V$ is defined as the density of superconducting electrons. The result is in agreement with Eq. (1.6).

Chapter 2

Superconducting qubits

2.1 Josephson junctions and Josephson effect

In 1962 Brian David Josephson demonstrated theoretically that Cooper pairs can tunnel through a barrier generating a current [20]. The tunneling of normal-conducting electrons was a well-known fact [21, 22], but the tunneling of an electron pair was never observed. One year after Josephson's paper, Anderson and Rowell claimed to have observed experimentally such an effect [23].
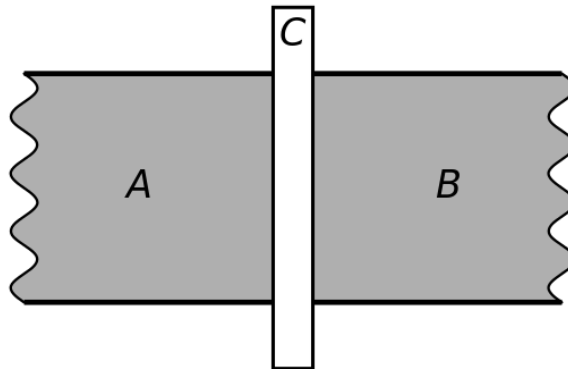

Figure 2.1: Schematic of a Josephson junction. A,B are the superconductors and C is the insulating layer. From https://commons.wikimedia.org/wiki/File:Single_josephson_junction.svg [accessed 31 Aug, 2021].

Josephson junctions are devices in which two or more superconductors are coupled by a thin layer of insulating material. By connecting the junction to an external circuit it is possible to measure both the current and the voltage drop across the barrier. The difficulties in observing the Josephson tunneling phenomenon are due to the strong influence that temperature and magnetic fields have on the Cooper pairs.

We now proceed with the demonstration of some of the effects observed in a Josephson junction using a simple model. Two superconductors of the same material are connected as in Fig. 2.1 and the temperature of the setup is well below the critical temperature T_C: the electrons are thus in the BCS ground state. According to the Ginzburg-Landau theory [24], Cooper pairs can be described by a complex order parameter

$$\Psi_j = \sqrt{n_{cj}} \, e^{i\phi_j}, \tag{2.1}$$

in which n_{cj} is the density of Cooper pairs in the superconductor indexed by $j = A, B$ as in Fig. 2.1. The phases of the complex Ψ can be different on the two sides of the junction because of the weakness of the link represented by the barrier. Given the Hamiltonians $\hat{H}_j$ of the isolated superconductor and the coupling constant $\mathcal{T}$ of the tunnel junction, Ψ_j satisfy

$$i\hbar \frac{\partial \Psi_A}{\partial t} = \hat{H}_A \Psi_A + \mathcal{T} \Psi_B, \qquad\qquad i\hbar \frac{\partial \Psi_B}{\partial t} = \hat{H}_B \Psi_B + \mathcal{T} \Psi_A. \tag{2.2}$$

We now suppose the Ψ_j to be eigenstates of the Hamiltonians $\hat{H}_j$ and thus $\hat{H}_j \Psi_j = E_j^0 \Psi_j$. Because of

the symmetries of the model, $E_A^0 = E_B^0 \equiv E^0$ holds.

A voltage U applied across the junction causes an energy shift $\Delta E = E_A - E_B = q\, U$ between the two superconductors, with $q = -2e$ being the Cooper pair charge. Defining as zero the midpoint energy of the two superconductors, Eq. (2.2) simplifies to

$$i\hbar \frac{\partial \Psi_A}{\partial t} = \frac{q\, U}{2} \Psi_A + \mathcal{T}\Psi_B, \qquad\qquad i\hbar \frac{\partial \Psi_B}{\partial t} = -\frac{q\, U}{2} \Psi_B + \mathcal{T}\Psi_A. \qquad (2.3)$$

Inserting Eq. (2.1) into Eq. (2.3) and separating real parts and imaginary parts we get

$$\dot{n}_{cA} = \frac{2\mathcal{T}}{\hbar} \sqrt{n_{cA} n_{cB}} \sin\left(\phi_B - \phi_A\right), \qquad\qquad \dot{\phi}_A = -\frac{\mathcal{T}}{\hbar}\sqrt{\frac{n_{cB}}{n_{cA}}} \cos\left(\phi_B - \phi_A\right) - \frac{q\, U}{2\hbar}, \qquad (2.4)$$

$$\dot{n}_{cB} = -\frac{2\mathcal{T}}{\hbar} \sqrt{n_{cA} n_{cB}} \sin\left(\phi_B - \phi_A\right), \qquad\qquad \dot{\phi}_B = -\frac{\mathcal{T}}{\hbar}\sqrt{\frac{n_{cA}}{n_{cB}}} \cos\left(\phi_B - \phi_A\right) + \frac{q\, U}{2\hbar}.$$

Assuming $n_{cA} = n_{cB} \equiv n_c$ for symmetry considerations and defining the difference of wave function phases as $\delta = \phi_B - \phi_A$, Eq. (2.4) leads to

$$\dot{n}_{cA} + \dot{n}_{cB} = 0, \qquad\qquad \dot{\delta} = \dot{\phi}_B - \dot{\phi}_A = \frac{q\, U}{\hbar}. \qquad (2.5)$$

The first result of Eq. (2.5) confirms the conservation of the total number of Cooper pairs in the two superconductors, while the second result gives information about the oscillation of the quantities in Eq. (2.4), namely

$$\delta(t) = \delta_0 + \frac{q}{\hbar} \int_0^t U(\nu)\, d\nu, \qquad (2.6)$$

where δ_0 is the difference of the wave function phases at the initial time $t = 0$. We are interested in the case of a constant voltage U, thus the equation of the tunnel current has the form

$$J_{\mathcal{T}}(t) = \frac{2\mathcal{T} n_c}{\hbar} \sin\left(\delta_0 - \frac{2eU}{\hbar} t\right) = J_0 \sin\left(\delta_0 - \frac{2eU}{\hbar} t\right). \qquad (2.7)$$

Equation (2.7) summarizes the conclusions made by Josephson in his 1962 paper [20]. For finite voltages U, an alternating supercurrent occurs. That current has an amplitude of $J_0 = 2\mathcal{T} n_c/\hbar$ and a frequency of $f = 2eU/(2\pi\hbar) = 2eU/h$. Instead, for a vanishing voltage ($U = 0$) a direct current up to a maximum of J_0 occurs. The direction of this DC current and its magnitude depend on the value of δ_0.

2.2 Charge qubits

As seen in the previous section, below the critical temperature Josephson junctions allow the tunneling of Cooper pairs across the barrier. This process is dissipationless and maintains the coherence of the Cooper pair states under suitable conditions (e.g., low temperatures, external fields screening, etc.). Also, Josephson junctions can be embedded in electronic circuits and coupled with other Josephson junctions. Such properties suggest Josephson junctions as possible quantum devices to be used as *qubits*.

In quantum computing, a qubit is a two-level quantum system that represents the basic unit of quantum information. The qubit can be in the states $|0\rangle$, $|1\rangle$ or even in a coherent superposition of these two states, according to quantum mechanics. The manipulation of the qubit state is provided by the *qubit gates*. The implementation of these qubit gates depends on the setup chosen to represent the qubit. For instance, in Josephson junctions the necessary gates can be obtained by controlling applied voltages, magnetic fields and the coupling with other Josephson junctions.

We now focus on the specific setup of charge qubits [4]. A charge qubit consists of a small super-conducting island (the "box" in Fig. 2.2) connected by a thin insulator to a superconducting reservoir. Cooper pairs can tunnel through the insulator by the Josephson effect. The number n of excess Cooper pairs in the box, relatively to some reference state, is the degree of freedom of the system. The proper
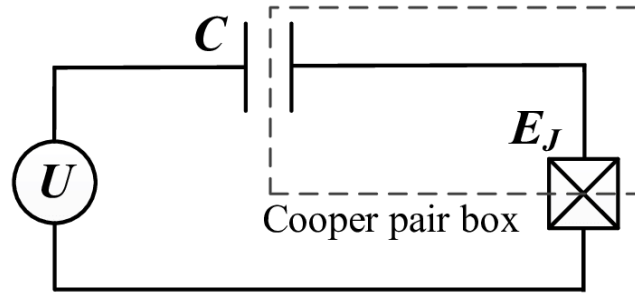
Figure 2.2: Schematic representation of a charge qubit. E_J is the Josephson energy, U is the gate voltage and C is the gate capacitance. The dashed rectangle represents the box with the excess of Cooper pairs [25, Figure 2].

choice of the experimental parameters allows to restrict n to a set of only two values, transforming the junction to a two-level quantum system, i.e., a qubit.

The tunnel junction has capacitance C_J, Josephson coupling energy E_J, and it is biased by an external controllable voltage U with gate capacitance C. The voltage U has the same role of the voltage of Sect. 2.1. In the arrangement of charge qubits, the charging energy of an electron is $E_C = e^2/2\,(C + C_J)$ and E_J is related to the maximum current that can flow through the tunnel junction without dissipation. In low-capacitance charge qubits the charging energy is greater than the Josephson energy by a factor of 10. Using junctions with capacitances $C_J \leq 10^{-15}$ F and gates with even smaller capacitances, charging energy is in the range $E_C/k_B \geq 1\,\mathrm{K}$ and consequently $E_J/k_B \sim 100\,\mathrm{mK}$. The superconducting material is the same on both sides and the energy gap Δ is larger than every characteristic energy of the system. At low temperatures the single-electron tunneling is exponentially suppressed, because an unpaired electron would cost an additional energy of Δ to the ground state energy. Under such conditions, only Cooper pairs tunnel through the barrier, and they tunnel coherently. The system is described by the Hamiltonian [4, 26]

$$\hat{H}_{1Q} = 4E_C \,(\hat{n} - n_g)^2 - E_J \cos\hat{\Theta}, \tag{2.8}$$

in which $\hat{n}$ is the number operator of excess Cooper-pair charges on the box and $\hat{\Theta}$ is the phase of the superconducting order parameter of the box. Operators $\hat{n}$ and $\hat{\Theta}$ are canonically conjugate, so $[\hat{\Theta}, \hat{n}] = i$ holds. The dimensionless gate charge $n_g = CU/2e$ can be controlled by tuning the value of the gate voltage U. For $E_C \gg E_J$ the Hamiltonian (2.8) can be conveniently written in the basis of eigenstates $|n\rangle$ of the number operator $\hat{n}$. The $\cos\hat{\Theta}$ term in this basis evaluates as

$$\cos\hat{\Theta}\,|n\rangle = \frac{1}{2}\left(e^{i\hat{\Theta}} + e^{-i\hat{\Theta}}\right)|n\rangle = \frac{1}{2}\left(|n+1\rangle + |n-1\rangle\right). \tag{2.9}$$

Hence, the Hamiltonian (2.8) in the $|n\rangle$-basis reads as

$$\hat{H}_{1Q} = \sum_n \left[4E_C \,(n - n_g)^2\,|n\rangle\langle n| - \frac{1}{2}E_J \left(|n+1\rangle\langle n| + |n\rangle\langle n+1|\right)\right]. \tag{2.10}$$

The Hamiltonian (2.10) is, with good approximation, diagonal in the $|n\rangle$-basis for almost every value of n_g because $E_C \gg E_J$. Thus, the charge states $|n\rangle$ are weakly mixed by the E_J-term. An important exception is the case of half-integer n_g. Indeed, if n_g is half-integer the charging energies of the two states $|n_g - \frac{1}{2}\rangle$ and $|n_g + \frac{1}{2}\rangle$ are equal and the E_J-term mixes strongly the two states. At low temperatures ($T \ll E_C/k_B$) the dynamic of the system is limited to these two states. We assume $n_g \in [0, 1]$ in the following calculations. The Hamiltonian (2.10), written in spin-1/2 notation and restricted to the states $|0\rangle, |1\rangle$, simplifies to

$$\hat{H}_{1Q} = -\frac{1}{2}B_z\hat{\sigma}_z - \frac{1}{2}B_x\hat{\sigma}_x, \tag{2.11}$$

in which we defined

$$|0\rangle = \begin{pmatrix} 1 \\ 0 \end{pmatrix}, \qquad\qquad \hat{\sigma}_z = \begin{pmatrix} 1 & 0 \\ 0 & -1 \end{pmatrix}, \qquad\qquad B_z = 4E_C(1 - 2n_g), \qquad (2.12)$$

$$|1\rangle = \begin{pmatrix} 0 \\ 1 \end{pmatrix}, \qquad\qquad \hat{\sigma}_x = \begin{pmatrix} 0 & 1 \\ 1 & 0 \end{pmatrix}, \qquad\qquad B_x = E_J.$$

The spin-1/2 notation has the quality of describing any two-state quantum system with an Hamiltonian $\hat{H}(t) = -\frac{1}{2}\boldsymbol{B}(t) \cdot \hat{\boldsymbol{\sigma}}$, where $\hat{\sigma}_{x,y,z}$ are Pauli matrices. The implementation of charge qubits allows to tune the $\hat{\sigma}_z$-term of $\hat{H}_{1Q}$ by controlling the gate voltage U, while the $\hat{\sigma}_x$-term is fixed by the value of Josephson charging energy E_J. However, a setup that uses two Josephson junctions in a loop configuration allows the tuning of E_J by controlling an external flux Φ_x in the center of the loop [4, Sect. IIB]. By controlling both B_x and B_z it is possible to implement all of the one-qubit logic gates.

In order to obtain two-qubit logic gates we need to couple qubits in pairs and to control the interactions between them. This operation can be achieved by connecting with a capacitor the superconducting boxes of two qubits[1]. The resulting charge-charge interaction can be described by a $\hat{\sigma}_z^1\hat{\sigma}_z^2$-term in the Hamiltonian. With a controlled inter-qubit interaction of this type, we will see in Sect. 2.3 that it is possible to realize easily the controlled-NOT gate. The Hamiltonian of two coupled qubits is thus

$$\hat{H}_{2Q} = -\frac{1}{2}B_z^1\hat{\sigma}_z^1 - \frac{1}{2}B_x^1\hat{\sigma}_x^1 - \frac{1}{2}B_z^2\hat{\sigma}_z^2 - \frac{1}{2}B_x^2\hat{\sigma}_x^2 + E_{CC}\,\hat{\sigma}_z^1\hat{\sigma}_z^2. \qquad (2.13)$$

The parameter E_{CC} represents the tunable Coulomb charging energy associated to the qubits. The ability to tune $B_x^{1,2}$, $B_z^{1,2}$, E_{CC} allows us to implement a universal set of gates.

2.3   Implementation of qubit gates

Here we show how to obtain the logic gates by tuning properly the charge qubit controls. The gates' symbols are defined without the hat to improve readability.

2.3.1   One-qubit gates

Using Eq. (2.11) we can calculate the one-qubit time-evolution operator

$$\hat{\mathcal{U}}_{1Q}(\tau) = \exp\left(-\frac{i\tau}{\hbar}\hat{H}_{1Q}\right) = \begin{pmatrix} \cos\frac{\tau\mathcal{B}}{2\hbar} + i\frac{B_z}{\mathcal{B}}\sin\frac{\tau\mathcal{B}}{2\hbar} & i\frac{B_x}{\mathcal{B}}\sin\frac{\tau\mathcal{B}}{2\hbar} \\ i\frac{B_x}{\mathcal{B}}\sin\frac{\tau\mathcal{B}}{2\hbar} & \cos\frac{\tau\mathcal{B}}{2\hbar} - i\frac{B_z}{\mathcal{B}}\sin\frac{\tau\mathcal{B}}{2\hbar} \end{pmatrix}, \qquad (2.14)$$

in which we defined $\mathcal{B} = \sqrt{(B_x)^2 + (B_z)^2}$. This operator represents the most general one-qubit gate that can be obtained by a quantum state evolution of time τ when the charge-qubit parameters n_g and E_J are fixed.

A rotation of angle α around the x-axis is described by the matrix

$$U_x(\alpha) = \begin{pmatrix} \cos\frac{\alpha}{2} & i\sin\frac{\alpha}{2} \\ i\sin\frac{\alpha}{2} & \cos\frac{\alpha}{2} \end{pmatrix}, \qquad (2.15)$$

and it can be obtained from Eq. (2.14) by setting $B_z = 0$. This result can be achieved in the simplest implementation of charge qubits by setting $n_g = 1/2$, i.e., by switching on an external voltage $U = e/C$, for a timespan of τ. The Josephson energy E_J is fixed under such assumption. To obtain the desired α-rotation the time of evolution has to be set to $\tau = \hbar\alpha/E_J$ if $E_J > 0$. Typical timespans of this implementation are in the range of 0.1 ns for $E_J/k_B \sim 100\,\mathrm{mK}$.

A z-rotation of angle β is instead described by

$$U_z(\beta) = \begin{pmatrix} e^{i\beta/2} & 0 \\ 0 & e^{-i\beta/2} \end{pmatrix}, \qquad (2.16)$$

---

[1]Although leading to easy theoretical calculations, the switches used in the implementation of this qubit interaction introduce strong dephasing effects. So, different types of coupling are usually used in the experiments.

and the corresponding qubit gate is obtained by setting $B_x = 0$ in the time evolution operator $\hat{\mathcal{U}}_{1Q}(\tau)$. It is possible to approximately implement such gate in charge qubits since $E_C \gg E_J$. The gate voltage U could be, for instance, set at 0, so that also $n_g = 0$ and $B_z = 4E_C \gg E_J = B_x$ holds. The rotation of an angle β around the z-axis is then achieved by setting $\tau = \hbar\beta/(4E_C)$. For $E_C/k_B \geq 1\,\mathrm{K}$ this implementation has typical timespans of $\tau \lesssim 1\,\mathrm{ps}$. With a more complicated setup $B_x = 0$ can be achieved by tuning exactly $E_J = 0$.

Using combinations of x- and z-rotations, it is possible to obtain all the one-qubit gates. The NOT gate

$$\mathrm{NOT} = \begin{pmatrix} 0 & 1 \\ 1 & 0 \end{pmatrix}, \tag{2.17}$$

is equivalent to a π-rotation around the x-axis up to a global phase factor of i. While the Hadamard gate

$$H = \frac{1}{\sqrt{2}} \begin{pmatrix} 1 & 1 \\ 1 & -1 \end{pmatrix}, \tag{2.18}$$

needs three rotations if B_x and B_z cannot be switched on simultaneously, as it is the case of the simple charge qubit implementation. Indeed,

$$H \propto U_x(\pi/4)\, U_z(\pi/4)\, U_x(\pi/4). \tag{2.19}$$

The ability to simultaneously switch $B_x = B_z$ for a time $\tau = \hbar\pi/B_x$ allows an easier and faster implementation of the Hadamard gate. In the charge qubit setup these controls can be achieved by fixing a value of E_J and by setting the external voltage U so that $n_g = \frac{1}{2} - \frac{E_J}{8E_C}$. The time of evolution is thus $\tau = \hbar\pi/E_J$ in this implementation.

2.3.2 Two-qubit gates

The two-qubit time-evolution operator is defined similarly as

$$\hat{\mathcal{U}}_{2Q}(\tau) = \exp\left(-\frac{i\tau}{\hbar}\hat{H}_{2Q}\right), \tag{2.20}$$

but the characterization of its general form is outside of the scope of this thesis. Indeed, the CNOT gate is the only two-qubit gate we are interested in, since the other two-qubit gates can be obtained with only one-qubit operations. The $\hat{\sigma}_z^1\hat{\sigma}_z^2$-coupling of the Hamiltonian (2.13) allows the implementation of CNOT gate with only a two-qubit operation [4, Appx. B3],

$$\mathrm{CNOT} \propto H^2 \left[U_z^1(-\pi/2)\, U_z^2(-\pi/2)\, \exp\left(i\frac{\pi}{4}\hat{\sigma}_z^1\hat{\sigma}_z^2\right) \right] H^2, \tag{2.21}$$

in which H^2 is the Hadamard gate applied to the qubit 2. Supposing we have a system in which the Coulomb charging energy E_{CC} is negative, the $\exp\left(i\frac{\pi}{4}\hat{\sigma}_z^1\hat{\sigma}_z^2\right)$-term in the CNOT implementation can be obtained by tuning the inter-qubit coupling for a timespan $\tau = \hbar\pi/(4|E_{CC}|)$ while setting $E_J = 0$ and $n_g = 0$ for both qubits.

Chapter 3

Quantum Optimal Control

3.1 QOC Theory

Quantum Optimal Control applies OC-solutions to drive the evolution of a quantum system in a fixed time τ. The goal of this process is to obtain, at the end of the time evolution, a final state with the desired properties. A QOC problem is completely defined in terms of the system dynamics, the control objectives, and the control space restrictions [27]. The evolution of pure states is described by the Schrödinger equation. A generalized equation holds for the evolution of mixed states. The Hamiltonian that describes the system dynamics is decomposed into a constant drift Hamiltonian $\hat{H}_d$ and a time-dependent control Hamiltonian $\hat{H}_c(t) = \sum_i u_i(t)\hat{H}_{i,c}$ in which the control pulses $u_i(t)$ enters as a constant factor input of Hamiltonians $\hat{H}_{i,c}$. The control objectives are defined in terms of a function J, the *cost function* or *figure of merit*. The ultimate goal of QOC is to find the control pulses $u_i(t)$ that minimize J. The optimal control pulses will be, then, applied in the experiments to get the desired evolution. The cost function evaluates numerically how the evolution controlled by the pulses $u_i(t)$ satisfies the goal of the optimization. For example, at the end of the evolution of a state $|\psi\rangle$ into a state $|\psi(\tau)\rangle$, J evaluates the distance between $|\psi(\tau)\rangle$ and a target state $|\psi_t\rangle$ computing $J = 1 - |\langle\psi_t|\psi(\tau)\rangle|^2$. Similarly, J can evaluate the distance between an evolved gate $U(\tau)$ and a target one U_t. The cost function can also encode physical restrictions, e.g., limitations on the power of the control pulses, limitations on the bandwidth, etc. For example, when a control pulse exceeds the restrictions, a penalty term is added to J. More direct restrictions on the control pulses can be realized by adding limitations to the pulses, such as hard walls, or by squeezing the control pulses.

Numerical algorithms used in QOC can be divided in gradient-based and gradient-free algorithms. On one side, gradient-based algorithms compute at each iteration the derivative of the cost function J with respect to the control pulses $u_i(t)$. The control pulses are then updated following the direction of the functional derivative. The use of small steps in the algorithm guarantees the improvement of J. On the other side, gradient-free algorithms allow an improvement of J without calculating its gradient. This feature is particularly important for optimizations in which the evaluation of the gradient of J is expensive or even impossible.

3.1.1 CRAB algorithm

The Chopped RAndom Basis (CRAB) gradient-free algorithm uses a truncated randomized basis of functions in order to simplify the minimization of the cost function J [27, 28]. The algorithm recasts the problem of functional minimization to a multi-variable function minimization exploiting the advantages of a randomized basis of functions. In the following we focus on the basis of trigonometric functions. Fixing the number of basis elements N_{be} and the evolution time τ, a possibility to randomize our trigonometrical basis is to choose the N_{be} frequencies according to

$$\omega_i = \frac{2\pi}{\tau}\left(i - r_i\right), \tag{3.1}$$

with $i = 1, \ldots, N_{be}$ [27]. The numbers r_i are picked randomly from a flatten distribution in $[0, 1]$. Equation (3.1) is the definition used in the optimizations of Sect. 3.2, although in principle other

definitions of the random frequencies ω_i can be chosen. The time-dependent control pulse can be thus written as

$$u(t) = \sum_{i=1}^{N_{be}} \left[A_i \sin(\omega_i t) + B_i \cos(\omega_i t) \right]. \tag{3.2}$$

The cost function depends now on the amplitudes A_i, B_i and at every iteration the minimizing algorithm computes J straightforwardly. A direct search method such as Nelder-Mead [29] updates the amplitudes (i.e. the control pulse) after each iteration. When the updated control pulse fulfils the algorithm stopping criteria, the optimal control pulse is obtained.

A more advanced version of the algorithm, the dressed Chopped RAndom Basis algorithm, or dCRAB, repeats the CRAB routine several times [30]. At every repetition of the CRAB algorithm, the so-called superiteration, a new set of frequencies is chosen and the optimal pulse is found. The initialization pulse for every superiteration is chosen to be equal to the optimal pulse of the previous superiteration. The final control pulse is given by the sum of the control pulses of all the superiterations. This improved algorithm allows to avoid the local minima of the cost function and needs less optimization parameter for every CRAB routine, i.e., for every superiteration. However, the CRAB algorithm turns out to be sufficient for the optimizations of Sect. 3.2 and the improvements of the dCRAB algorithm are not further exploited.

3.2 Application to superconducting qubits

In this section we show how the implementation of one- and two-qubit gates can be improved with QOC using the CRAB algorithm. We postulate the presence of dephasing effects from the external world and we try to find an optimal pulse that can compensate for these undesired effects. The optimization procedure is similar in both cases.

At first the Hamiltonian without external noise is defined. With this Hamiltonian we implement the target gate by switching on its drift part $\hat{H}_d$ for a precise amount of time τ. The evolution time τ is fixed during the optimization. By fixing τ we simulate the experimental situation in which the detuning source is constant, the pure states evolve according to Schrödinger equation, and the cost function J is computed from the experimental final state $|\psi(\tau)\rangle$. Then, the control pulses are updated following the optimization algorithm. On our side we can simulate numerically the evolution of $|\psi\rangle$ and then the process is equivalent to the experimental one.

In the following optimizations the gate cost function J is defined as

$$J = 1 - \frac{1}{N_0^2} \left| Tr(U_t^\dagger U(\tau)) \right|^2 = 1 - \frac{1}{N_0^2} \left| \sum_{i=1}^{N_0} \langle \zeta_i | U_t^\dagger | \phi_i(\tau) \rangle \right|^2. \tag{3.3}$$

In Eq. (3.3) $|\zeta_i\rangle$ are the basis states of the Hilbert space $\mathcal{H}$ of dimension $N_0 = \dim \mathcal{H}$. The states $|\phi_i(\tau)\rangle = U(\tau) |\zeta_i\rangle$ are obtained by integrating for a time τ the Schrödinger equation

$$i \frac{d}{dt} |\psi(t)\rangle = H(u_1(t), \dots, u_m(t)) |\psi(t)\rangle, \tag{3.4}$$

using $|\zeta_i\rangle$ as the initial state. In all the QOC calculations $\hbar = 1$ is intended. We highlight the dependence of the Hamiltonian on the time-dependent control pulses $u_i(t)$, $i = 1, \dots, m$. The cost function J defined as in Eq. (3.3) can be interpreted as an esteem of the *infidelity* of the gate, since if $U(\tau)$ tends to U_t then J tends to zero. The task of QOC is thus to minimize the gate cost function or, equivalently, the gate infidelity.

3.2.1 Optimization of one-qubit NOT gate

From Sect. 2.3.1 we know that the NOT gate can be obtained by letting the system evolve, according to the Hamiltonian

$$\hat{\hat{H}}_{1Q} = -\frac{1}{2} B_x \, \hat{\sigma}_x, \tag{3.5}$$

for a time $\tau = \pi/B_x$. The parameter B_x is positive and constant. In the following we define all the physical quantities relatively to B_x to get comparable results and to fix the timescales of the optimization. The numerical value of B_x is ultimately set to 1 and the time of evolution is thus $\tau = \pi$. In Fig. 3.1 it is possible to see that the NOT gate behaves as expected if the system is described exactly by the Hamiltonian (3.5). Small bars are still visible in the diagonal elements of Fig. 3.1 because of the finite precision of the integration method. We calculate the value of J as in Eq. (3.3) to have an estimate of the implemented gate infidelity.

However, in the real implementation of a NOT gate the Hamiltonian that describes the system could be different from what we expect. Additional terms in the Hamiltonian (3.5) can arise from external sources that we can not control. For example, we can model the system by considering in the Hamiltonian (3.5) an additional $\hat{\sigma}_z$-term, i.e.,

$$\hat{H}_{1Q}^* = -\frac{1}{2} B_x \hat{\sigma}_x + \beta \hat{\sigma}_z. \tag{3.6}$$

The magnitude of this additional term is fixed to $\beta = 0.2\, B_x$. In this thesis, the "noise" is defined as an additional term in the Hamiltonian that deviates the time evolution of a system from the expected one. The time evolution described by the noisy Hamiltonian (3.6) for a time $\tau = \pi/B_x$ leads to the gate represented in Fig. 3.2.

Tomography of Ideal NOT Gate

Tomography of Noisy NOT Gate
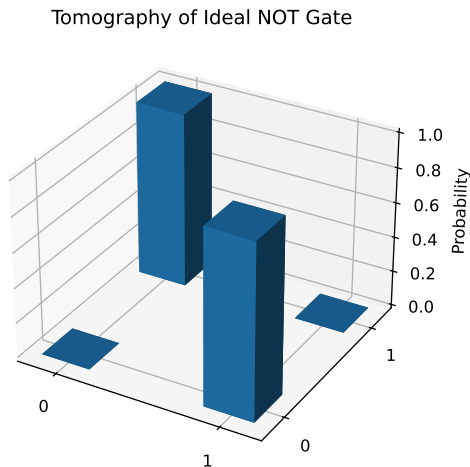
Figure 3.1: Tomography of the NOT gate in the noiseless approximation. The blue bars represent the probabilities of the corresponding matrix element. The gate infidelity of this implementation is $J = 3.8 \cdot 10^{-15}$.
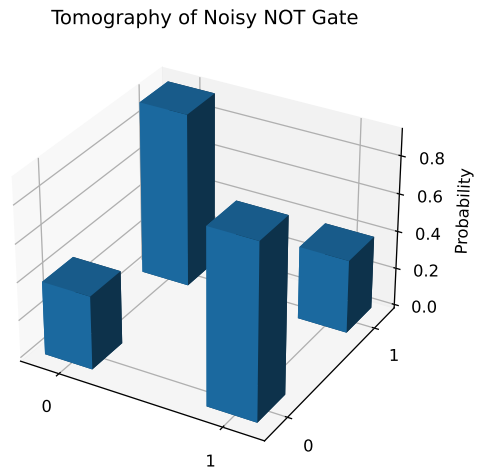
Figure 3.2: Tomography of the noisy NOT gate. The gate infidelity of this implementation is $J = 0.15$.

To improve the implementation of the noisy NOT gate, we add to the Hamiltonian (3.6) a time-dependent control pulse that generates a rotation around the x-axis. The controlled Hamiltonian is thus

$$\hat{H}_{1Q}(t) = \hat{H}_{1Q}^* + B_x \sum_{i=1}^{N_{be}} [A_i \sin(\omega_i t) + B_i \cos(\omega_i t)] \, \hat{\sigma}_x. \tag{3.7}$$

The definition of the control pulse parameters is reported in Sect. 3.1.1.
In the following one-qubit gate optimization the number of frequencies is set to $N_{be} = 3$. The random frequencies are chosen according to Eq. (3.1). The $2N_{be}$ initialization amplitudes are picked up randomly in the (arbitrary) interval $\left[-\frac{1}{2}, \frac{1}{2}\right]$ to set a large initial step to escape local minima.
We then employ the Nelder-Mead algorithm [29] to find the amplitudes A_i, B_i that minimize the cost function J. The algorithm starts by transforming the initialization amplitudes into the $2N_{be}$-dimensional initialization simplex. One vertex of this simplex is the origin, while the others $2N_{be}$ are generated by translating the origin along each dimension according to the corresponding initial amplitude. Each step of the algorithm computes a new simplex performing reflections, expansions,

contractions, and shrinks, using a fixed characteristic parameter for each of these operations. The algorithm computes the value of J for every new vertex found by these operations. The algorithm returns the final amplitudes when one of the convergence criteria is met. We considered three convergence criteria: the maximum number of function evaluations, the maximum number of algorithm iterations, and the difference of both amplitudes and cost function values below a specific tolerance. The first two criteria halt the algorithm if it is requiring excessive time, while the third criterion stops the algorithm when an acceptable precision on the final result is obtained. To be more specific, at every iteration the vertex with the lowest value of J is selected and the differences of its function value and the function values of the other vertices are computed. If all of these differences are below the tolerance value f_{tol}, a similar control is done to the coordinates of all the other vertices with respect to the best vertex. If also all of these differences are below the tolerance value x_{tol}, the algorithm stops successfully and returns the coordinates (i.e., the amplitudes) of the vertex with the lowest value of J. In the next optimization we set the maximum number of iterations and the maximum number of function evaluations at 1200, while we fix $x_{tol} = 10^{-4}$ and $f_{tol} = 10^{-4}$.
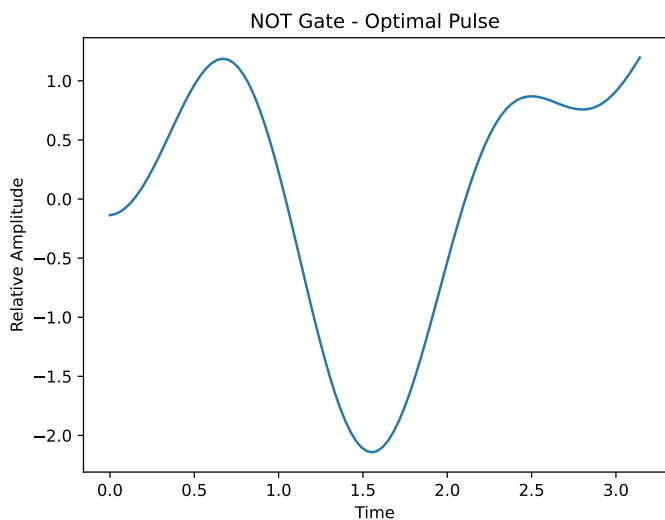
Figure 3.3: Optimal pulse found by a run of the algorithm. The total time of the pulse is set to π and the amplitude on the y-axis is relative to the value of B_x.
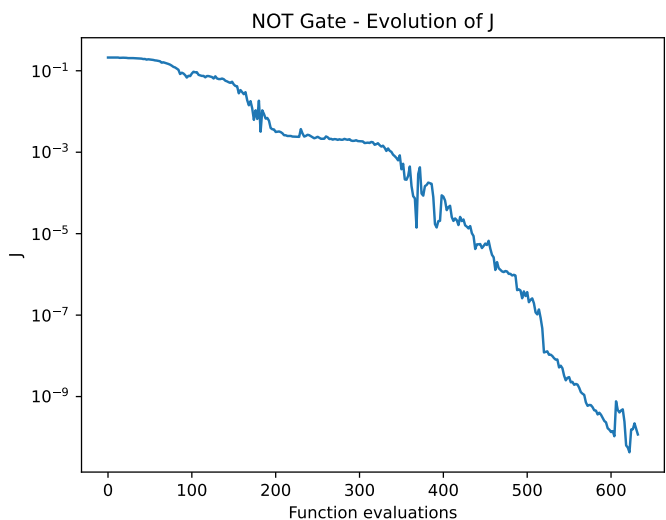
Figure 3.4: Evolution of the gate cost function J (in logarithmic scale) over the number of the function evaluations. Only a value of J every 2 evaluations is shown. The final value of the infidelity is $J = 2.8 \cdot 10^{-11}$.

Figure 3.3 shows a typical pulse obtained by the algorithm, while in Fig. 3.4 it is shown in chronological order what are the different function values tested by the algorithm. The spikes indicate vertex guesses that are worse than the vertices already found. The algorithm does not update the simplex in that case, but tries to find a better guess.

3.2.2 Optimization of two-qubit CNOT gate

We know from Eq. (2.21) that the CNOT gate can be obtained by switching on the inter-qubit coupling for a specific timespan and by performing 4 single-qubit operations. We focus only on the optimization of the operations in the square brackets of Eq. (2.21), while the application of the Hadamard gates to the second qubit is considered as perfect and instantaneous. We have, then, to implement only the two-qubit operation $\exp\left(i\frac{\pi}{4}\hat{\sigma}_z^1\hat{\sigma}_z^2\right)$ and, for both qubits, the z-rotation $U_z(-\pi/2) \equiv U_z(3\pi/2)$. This implementation is possible considering the Hamiltonian

$$\hat{\tilde{H}}_{2Q} = -\frac{1}{2}B_z^1\hat{\sigma}_z^1 - \frac{1}{2}B_z^2\hat{\sigma}_z^2 + E_{CC}\,\hat{\sigma}_z^1\hat{\sigma}_z^2. \tag{3.8}$$

Both $B_z^{1,2}$ and E_{CC} are defined relatively to a positive parameter B_x and they can be tuned to realize different operations on the qubits. The implementation of the CNOT gate proceeds in two different

steps:

1. The two-qubit operation $\exp\left(i\frac{\pi}{4}\hat{\sigma}_z^1\hat{\sigma}_z^2\right)$ is performed. We fix the inter-qubit coupling to $E_{CC} = -0.1\,B_x$ and we set $B_z^1 = B_z^2 = 0$. The evolution time of this step is $\tau_1 = \pi/(4\,|E_{CC}|) = \pi/(0.4\,B_x)$.

2. The one-qubit operation $U_z(3\pi/2)$ is realized for each qubit. We set $E_{CC} = 0$ and we fix $B_z^1 = B_z^2 = -B_x$ instead. The evolution time of this step is $\tau_2 = \pi/(2\,B_x)$.
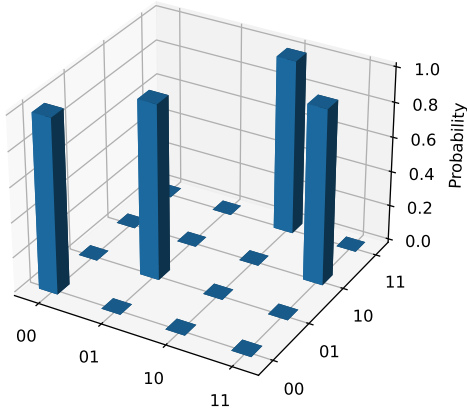

Tomography of Ideal CNOT Gate

Tomography of Noisy CNOT Gate

Figure 3.5: Tomography of the CNOT gate in the noiseless approximation. The gate infidelity of this implementation is $J = 2.8 \cdot 10^{-13}$.
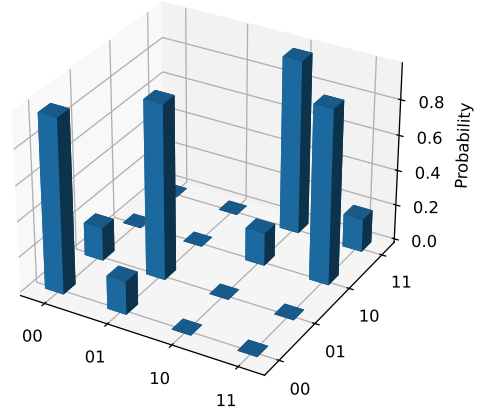
Figure 3.6: Tomography of the noisy CNOT gate. The gate infidelity of this implementation is $J = 0.069$.

The value of B_x is set to 1 as in the one-qubit optimization.

In Fig. 3.5 it is shown the aforementioned implementation if the system Hamiltonian is exactly (3.8). This implementation is similar to the target gate to a very good approximation. We can consider, now, two additional terms in the Hamiltonian (3.8) that disturb the expected time evolution, for example

$$\hat{H}_{2Q}^* = -\frac{1}{2}B_z^1\hat{\sigma}_z^1 - \frac{1}{2}B_z^2\hat{\sigma}_z^2 + E_{CC}\,\hat{\sigma}_z^1\hat{\sigma}_z^2 + \beta\hat{\sigma}_z^1 + \beta\hat{\sigma}_z^2. \tag{3.9}$$

These additional terms act on the qubits with the same magnitude $\beta = -0.02\,B_x$ and lead to the gate represented in Fig. 3.6. These terms are present in both of the two implementation steps described above and they act on the system for a total time of $\tau_1 + \tau_2$. The obtained gate behaves differently from the target CNOT gate, so we add controls to the Hamiltonian (3.9) to direct its time evolution towards the desired CNOT gate.

We optimize the implementation of the two steps described above, while we still consider the application of the Hadamard gate as perfect and instantaneous. In other words, we optimize only the gate

$$U_z^1(-\pi/2)\,U_z^2(-\pi/2)\,\exp\left(i\frac{\pi}{4}\hat{\sigma}_z^1\hat{\sigma}_z^2\right), \tag{3.10}$$

from which the CNOT gate can be easily obtained. This goal can be achieved by defining a controlled Hamiltonian of the form

$$\hat{H}_{2Q}(t) = \hat{H}_{2Q}^* + \frac{1}{2}B_x\,u_1(t)\,\hat{\sigma}_z^1\hat{\sigma}_z^2 + B_x\,u_2(t)\,\left(\hat{\sigma}_x^1 + \hat{\sigma}_x^2\right), \tag{3.11}$$

where

$$u_1(t) = \sum_{i=1}^{N_{be}}\left[A_i\sin(\omega_i t) + B_i\cos(\omega_i t)\right], \qquad u_2(t) = \sum_{i=1}^{N_{be}}\left[C_i\sin(\omega_i t) + D_i\cos(\omega_i t)\right]. \tag{3.12}$$

The symmetries of this implementation suggest to use the same $\hat{\sigma}_x$-pulse on the two qubits, reducing the computational cost of the optimization. The random frequencies ω_i are the same for the $\hat{\sigma}_z^1 \hat{\sigma}_z^2$ and the $(\hat{\sigma}_x^1 + \hat{\sigma}_x^2)$ control pulses, but in general different frequencies can be chosen.
The two pulses $u_1(t), u_2(t)$ act on the system for the entire time needed by the two-step implementation, i.e., for a total time $\tau_1 + \tau_2 = 3\pi/B_x = 3\pi$ if $B_x = 1$. We write these two pulses in a truncated trigonometrical basis of $N_{be} = 5$ randomized frequencies. The frequencies are chosen according to (3.1). The $4N_{be}$ initialization amplitudes are selected randomly in $\left[-\frac{1}{2}, \frac{1}{2}\right]$. We employ the Nelder-Mead algorithm[1] with adaptive parameters [29, 31], which is specific for high-dimensional functions minimization.
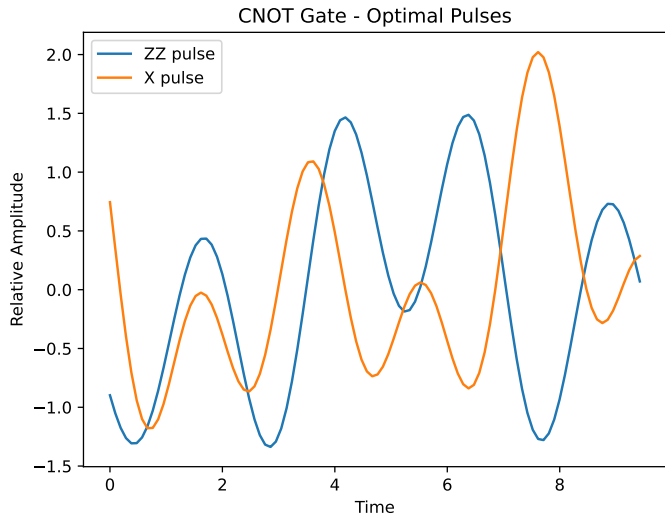
Figure 3.7: Optimal pulses found by a run of the algorithm. The total time of the pulses is set to 3π. The amplitudes on the y-axis correspond to $u_1(t)$ for the zz-pulse and to $u_2(t)$ for the x-pulse.
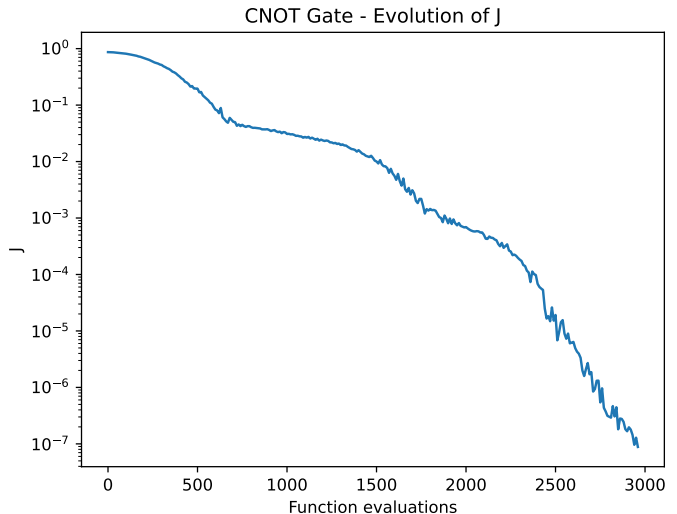
Figure 3.8: Evolution of the gate cost function J (in logarithmic scale) over the number of the function evaluations. Only a value of J every 10 evaluations is shown. The final value of the infidelity is $J = 8.7 \cdot 10^{-8}$.

Figure 3.7 shows the two pulses computed by the optimization algorithm, while the evolution of the value of J over the number of function evaluations is shown in Fig. 3.8. Here we point out the difference in the function evaluations between the two types of optimization we have performed. The higher number of dimensions of the two-qubit cost function with respect to the one-qubit cost function leads to more expensive computations. Indeed, our two-qubit optimization requires about five times more function evaluations than our single-qubit one. The final value of the gate infidelity is also three orders of magnitude greater in the two-qubit optimization than in one-qubit.
Similar difficulties are found experimentally: the setup that implements a two-qubit gate is longer to prepare and needs more time to evolve to the desired one. Thus, if decoherence times are limited, in the software development the number of two-qubit operations performed should be minimized. Nevertheless, two-qubit gates are fundamental building blocks of quantum computation and they can not be excluded from quantum algorithms.

---

[1]We set the maximum number of iterations and the maximum number of function evaluations at 6000, we fix $f_{\text{tol}} = 10^{-4}$ and we reduce x_{tol} to 10^{-3} to speed up the optimization.

Conclusions

In this thesis, we presented an application of quantum optimal control to one- and two-qubit gates based on superconducting qubits.

We presented at first the theory of superconductivity, focusing on the microscopical theory that explains the superconductivity phenomena. We highlighted two important concepts of the theory: Cooper pairs and superconducting energy gap.

Then, we reviewed how macroscopic quantum effects manifest themselves in Josephson junctions at low temperatures. In particular, the tunneling of Cooper pairs across the barrier maintains the coherence of the pairs' wave function at temperatures below the critical one and for setups with characteristic energies below the superconducting energy gap. We showed which experimental conditions are required to implement a quantum computing device based on superconducting Josephson junctions. The implementation of a charge qubit was presented in detail, while a possible improvement of the setup was mentioned. With this improvement, we can handle both x- and z-rotations of the charge qubit states, allowing us to realize all the one-qubit gates. Moreover, a possible solution to couple two qubits was briefly mentioned. Then, we presented how to obtain in practice the most common one-qubit gates and the CNOT gate by tuning charge qubit controls and by setting evolution times accordingly.

An improvement of the qubit gates implementation based on quantum optimal control was discussed. We described the theory of quantum optimal control, focusing on the Chopped RAndom Basis algorithm, and we applied such theory to the optimization of qubit gates. We defined the cost function to be minimized and we explained its connection to the gate infidelity. In other words, we showed how to estimate numerically the infidelity of a gate. We explained in details the minimization algorithm that was used in the optimization. The infidelity of a NOT gate was reduced by ten orders of magnitude by adding an additional control term in the Hamiltonian of the qubit. In other terms, the cost function of the NOT gate decreased by a factor of 10^{10}. Similarly, the CNOT gate infidelity was reduced by six orders of magnitude thanks to the optimized control pulses.

In conclusion, quantum optimal control can, theoretically, enhance the performances of existing gate implementations using software-based solutions. In our optimizations we achieved great improvements in the performances. However, these optimizations are only a first step towards the optimization of more complex systems, described by more general equations and disturbed by more general external dephasing sources, until we will be able to optimize real-world quantum systems.

Bibliography

[1] Richard P. Feynman. "Simulating physics with computers". In: *International Journal of Theoretical Physics* 21.6 (June 1982), pp. 467–488. ISSN: 1572-9575. DOI: 10.1007/BF02650179. URL: https://doi.org/10.1007/BF02650179.

[2] J. S. Bell. "On the Einstein Podolsky Rosen paradox". In: *Physics Physique Fizika* 1.3 (Nov. 1964), pp. 195–200. DOI: 10.1103/PhysicsPhysiqueFizika.1.195. URL: https://link.aps.org/doi/10.1103/PhysicsPhysiqueFizika.1.195.

[3] Don Coppersmith. "An approximate Fourier transform useful in quantum factoring". In: *arXiv preprint quant-ph/0201067* (2002). URL: http://arxiv.org/abs/quant-ph/0201067.

[4] Yuriy Makhlin, Gerd Schön, and Alexander Shnirman. "Quantum-state engineering with Josephson-junction devices". In: *Rev. Mod. Phys.* 73.2 (May 2001), pp. 357–400. DOI: 10.1103/RevModPhys.73.357. URL: https://link.aps.org/doi/10.1103/RevModPhys.73.357.

[5] Davide Castelvecchi. "Quantum computers ready to leap out of the lab in 2017". In: *Nature* 541.7635 (Jan. 2017), pp. 9–10. ISSN: 1476-4687. DOI: 10.1038/541009a. URL: https://doi.org/10.1038/541009a.

[6] Davide Castelvecchi. "IBM's quantum cloud computer goes commercial". In: *Nature* 543.7644 (Mar. 2017), pp. 159–159. ISSN: 1476-4687. DOI: 10.1038/nature.2017.21585. URL: https://doi.org/10.1038/nature.2017.21585.

[7] Rigetti Computing. *Rigetti Computing introduces world's first scalable multi-chip quantum processor.* https://www.globenewswire.com/news-release/2021/06/29/2255028/0/en/Rigetti-Computing-introduces-world-s-first-scalable-multi-chip-quantum-processor.html. [accessed 30 Aug, 2021]. June 2021.

[8] Frank Arute et al. "Quantum Supremacy using a Programmable Superconducting Processor". In: *Nature* 574 (2019), 505–510. URL: https://www.nature.com/articles/s41586-019-1666-5.

[9] James Sanders. *D-Wave announces 5,000-qubit fifth generation quantum annealer.* https://www.techrepublic.com/article/d-wave-announces-5000-qubit-fifth-generation-quantum-annealer/. [accessed 30 Aug, 2021]. Sept. 2019.

[10] J Werschnik and E K U Gross. "Quantum optimal control theory". In: *Journal of Physics B: Atomic, Molecular and Optical Physics* 40.18 (Sept. 2007), R175–R211. DOI: 10.1088/0953-4075/40/18/r01. URL: https://doi.org/10.1088/0953-4075/40/18/r01.

[11] Steffen J. Glaser et al. "Training Schrödinger's cat: quantum optimal control". In: *The European Physical Journal D* 69.12 (Dec. 2015), p. 279. ISSN: 1434-6079. DOI: 10.1140/epjd/e2015-60464-1. URL: https://doi.org/10.1140/epjd/e2015-60464-1.

[12] U. Boscain, M. Sigalotti, and D. Sugny. *Introduction to the Foundations of Quantum Optimal Control.* 2020. arXiv: 2010.09368 [quant-ph].

[13] H. Kamerlingh Onnes. "Further experiments with liquid helium. C. On the change of electric resistance of pure metals at very low temperatures etc. IV. The resistance of pure mercury at helium temperatures". In: *Through Measurement to Knowledge: The Selected Papers of Heike Kamerlingh Onnes 1853–1926*. Ed. by Kostas Gavroglu and Yorgos Goudaroulis. Dordrecht: Springer Netherlands, 1991, pp. 261–263. ISBN: 978-94-009-2079-8. DOI: 10.1007/978-94-009-2079-8_15. URL: https://doi.org/10.1007/978-94-009-2079-8_15.

[14] F. London, H. London, and Frederick Alexander Lindemann. "The electromagnetic equations of the supraconductor". In: *Proceedings of the Royal Society of London. Series A - Mathematical and Physical Sciences* 149.866 (1935), pp. 71–88. DOI: `10.1098/rspa.1935.0048`. eprint: `https://royalsocietypublishing.org/doi/pdf/10.1098/rspa.1935.0048`. URL: `https://royalsocietypublishing.org/doi/abs/10.1098/rspa.1935.0048`.

[15] R Meservey and BB Schwartz. "Equilibrium properties: Comparison of experimental results with predictions of the BCS theory". In: *Superconductivity*. CRC Press, 2018, pp. 117–191. DOI: `10.1201/9780203737965-3`. URL: `https://www.taylorfrancis.com/chapters/edit/10.1201/9780203737965-3/equilibrium-properties-comparison-experimental-results-predictions-bcs-theory-meservey-schwartz`.

[16] Leon N. Cooper. "Bound Electron Pairs in a Degenerate Fermi Gas". In: *Phys. Rev.* 104.4 (Nov. 1956), pp. 1189–1190. DOI: `10.1103/PhysRev.104.1189`. URL: `https://link.aps.org/doi/10.1103/PhysRev.104.1189`.

[17] J. Bardeen, L. N. Cooper, and J. R. Schrieffer. "Theory of Superconductivity". In: *Phys. Rev.* 108.5 (Dec. 1957), pp. 1175–1204. DOI: `10.1103/PhysRev.108.1175`. URL: `https://link.aps.org/doi/10.1103/PhysRev.108.1175`.

[18] H. Ibach and H. Lüth. *Solid-State Physics: An Introduction to Principles of Materials Science*. Advanced texts in physics. Springer Berlin Heidelberg, 2009. ISBN: 9783540938040. URL: `https://books.google.it/books?id=qjxv68JFe3gC`.

[19] L.E. Ballentine. *Quantum Mechanics: A Modern Development*. World Scientific, 1998. ISBN: 9789810241056. URL: `https://books.google.it/books?id=sHJRFHz1rYsC`.

[20] B.D. Josephson. "Possible new effects in superconductive tunnelling". In: *Physics Letters* 1.7 (1962), pp. 251–253. ISSN: 0031-9163. DOI: `https://doi.org/10.1016/0031-9163(62)91369-0`. URL: `https://www.sciencedirect.com/science/article/pii/0031916362913690`.

[21] M. H. Cohen, L. M. Falicov, and J. C. Phillips. "Superconductive Tunneling". In: *Phys. Rev. Lett.* 8.8 (Apr. 1962), pp. 316–318. DOI: `10.1103/PhysRevLett.8.316`. URL: `https://link.aps.org/doi/10.1103/PhysRevLett.8.316`.

[22] S. Shapiro et al. "Superconductivity and Electron Tunneling". In: *IBM Journal of Research and Development* 6.1 (1962), pp. 34–43. DOI: `10.1147/rd.61.0034`.

[23] P. W. Anderson and J. M. Rowell. "Probable Observation of the Josephson Superconducting Tunneling Effect". In: *Phys. Rev. Lett.* 10.6 (Mar. 1963), pp. 230–232. DOI: `10.1103/PhysRevLett.10.230`. URL: `https://link.aps.org/doi/10.1103/PhysRevLett.10.230`.

[24] Lev Davidovich Landau and V L Ginzburg. "On the theory of superconductivity". In: *Zh. Eksp. Teor. Fiz.* 20 (1950), p. 1064. URL: `http://cds.cern.ch/record/486430`.

[25] Rebing Wu et al. "Spectral Analysis and Identification of Noises in Quantum Systems". In: *Physical Review A* 87 (Nov. 2012). DOI: `10.1103/PhysRevA.87.022324`.

[26] Giuliano Benenti, Giulio Casati, and Giuliano Strini. *Principles of Quantum Computation and Information*. WORLD SCIENTIFIC, 2004. DOI: `10.1142/5528`. eprint: `https://www.worldscientific.com/doi/pdf/10.1142/5528`. URL: `https://www.worldscientific.com/doi/abs/10.1142/5528`.

[27] Phila Rembold et al. "Introduction to quantum optimal control for quantum sensing with nitrogen-vacancy centers in diamond". In: *AVS Quantum Science* 2.2 (2020), p. 024701. DOI: `10.1116/5.0006785`. eprint: `https://doi.org/10.1116/5.0006785`. URL: `https://doi.org/10.1116/5.0006785`.

[28] Tommaso Caneva, Tommaso Calarco, and Simone Montangero. "Chopped random-basis quantum optimization". In: *Physical Review A* 84.2 (Aug. 2011). ISSN: 1094-1622. DOI: `10.1103/physreva.84.022326`. URL: `http://dx.doi.org/10.1103/PhysRevA.84.022326`.

[29] J. A. Nelder and R. Mead. "A Simplex Method for Function Minimization". In: *The Computer Journal* 7.4 (Jan. 1965), pp. 308–313. ISSN: 0010-4620. DOI: 10.1093/comjnl/7.4.308. eprint: https://academic.oup.com/comjnl/article-pdf/7/4/308/1013182/7-4-308.pdf. URL: https://doi.org/10.1093/comjnl/7.4.308.

[30] N. Rach et al. "Dressing the chopped-random-basis optimization: A bandwidth-limited access to the trap-free landscape". In: *Physical Review A* 92.6 (Dec. 2015). ISSN: 1094-1622. DOI: 10.1103/physreva.92.062343. URL: http://dx.doi.org/10.1103/PhysRevA.92.062343.

[31] Fuchang Gao and Lixing Han. "Implementing the Nelder-Mead simplex algorithm with adaptive parameters". In: *Computational Optimization and Applications* 51.1 (Jan. 2012), pp. 259–277. ISSN: 1573-2894. DOI: 10.1007/s10589-010-9329-3. URL: https://doi.org/10.1007/s10589-010-9329-3.